IEEE Access
Multidisciplinary | Rapid Review | Open Access Journal

Received 14 September 2022, accepted 27 September 2022, date of publication 6 October 2022, date of current version 12 October 2022.

Digital Object Identifier 10.1109/ACCESS.2022.3211957

RESEARCH ARTICLE

3D Huygens Principle Based Microwave Imaging Through MammoWave Device: Validation Through Phantoms

BILAL KHALID[1], BANAFSHEH KHALESI[1,2,3], NAVID GHAVAMI[2,3], LORENZO SANI[2], ALESSANDRO VISPA[2], MARIO BADIA[2], SANDRA DUDLEY[1], MOHAMMAD GHAVAMI[1], (Senior Member, IEEE), AND GIANLUIGI TIBERI[1,2,3]

[1]School of Engineering, London South Bank University, SE1 0AA London, U.K.
[2]Umbria Bioengineering Technologies, 06081 Perugia, Italy
[3]UBT U.K. Division, W1B 3HH London, U.K.

Corresponding author: Bilal Khalid (khalidb4@lsbu.ac.uk)

This work was supported in part by the European Union's Horizon 2020 Research and Innovation Program under Grant 830265, (project MammoWave- Cutting edge microwave imaging device for safe and accurate breast cancer screening); in part by the European Union's Horizon 2020 Research and Innovation Program under the Marie Sklodowska-Curie grant agreement No. 872752, (project ROVER- Reliable Technologies and Models for Verified Wireless Body-centric Transmission and Localisation); and in part by the European Union's Horizon 2020 Research and Innovation Program under grant agreement No. 101017098 (Project RadioSpin- Deep Oscillatory Neural Networks Computing and Learning through the Dynamics of RF Neurons Interconnected by RF Spintronic Synapses).

ABSTRACT This work focuses on developing a 3D microwave imaging (MWI) algorithm based on Huygens principle (HP). Specifically, a novel, fast MWI device (MammoWave) has been presented and exploited for its capabilities of extending image reconstruction from 2D to 3D. For this purpose, dedicated phantoms containing 3D structured inclusion have been prepared with mixtures having different dielectric properties. Phantom measurements have been performed at multiple planes along the z-axis by simultaneously changing the transmitter and receiver antenna height via the graphic user interface (GUI) integrated with MammoWave. We have recorded the complex S21 multi-quote data at multiple planes along the z-axis. The complex multidimensional raw data has been processed via an enhanced HP based image algorithm for 3D image reconstruction. This paper demonstrates the successful detection and 3D visualization of the inclusion with varying dimensions at multiple planes/cross-sections along the z-axis with a dimensional error lower than 7.5%. Moreover, the paper shows successful detection and 3D visualization of the inclusion in a skull-mimicking phantom having a cylindrically shaped inclusion, with the location of the detected inclusion in agreement with the experimental setup. Additionally, the localization of a 3D structured spherical inclusion has been shown in a more complex scenario using a 3-layer cylindrically shaped phantom, along with the corresponding 3D image reconstruction and visualization.

INDEX TERMS Huygens principle (HP), MammoWave, microwave imaging (MWI), ultra-wideband (UWB).

I. INTRODUCTION

Medical imaging is a renowned technique to envisage the interior of the human body and plays a crucial role in segregating between healthy and diseased body parts and tissues. There are numerous imaging techniques, which are operating in medical oriented fields and generate images for treatment and diagnostics purposes. Medical imaging can be obtained from a variety of techniques i.e., x-rays, magnetic resonance imaging (MRI), ultrasound (US), computed tomography (CT), and positron emission tomography (PET). These techniques are usually expensive, need high maintenance and have bulky instruments difficult to reposition. Some techniques use ionized rays, which may cause health risks [1], [2]. Therefore, the health risks-free factor has led to the increased interest in the development of fast, novel, risk-free imaging technologies for diagnostic purposes.

The associate editor coordinating the review of this manuscript and approving it for publication was Mohamed Kheir.

Ultra-wideband (UWB) microwave imaging (MWI) is a promising technique securing many benefits in providing low-risk medical imaging of the internal organs and tissues of the human body, exploiting the contrast in dielectric properties. UWB was previously used for military purposes i.e., positioning and tracking. UWB started to gain researchers' attention since FCC issued the unlicensed use of UWB devices. UWB uses pulse-generated electromagnetic waves, which are non-ionizing in nature making it health risk-free for medical imaging. The pulses are generated for a very short interval making them operate under the allowed noise level, possessing high gain, speed, and precision. UWB impulses can easily penetrate through objects making them a prominent candidate for medical imaging [3], [4].

A wide range of research has been done in the past decade on microwave imaging and several imaging algorithms have been introduced and evolved with time, especially for breast lesion detection. Some of these microwave imaging algorithms are delay and sum (DAS), delay multiply and sum (DMAS), confocal imaging, robust capon beamforming (RCB) and channel ranked DAS (CR-DAS) [5], [6]. These mentioned MWI algorithms are radar techniques based on the time domain; they use real-time filters to compensate for fractional time delays. Alternatively, to radar techniques, microwave tomography techniques can be employed, but they may have drawbacks such as low signal to clutter and complex mathematical formulation [7]. Recently, more research has focused on developing new methodologies and evolving developed algorithms for 3-dimensional (3D) imaging. 3D medical imaging would be very useful for diagnostic purposes and for detecting the dimensions of the diseased parts and lesions. Examples of 3D MWI prototypes and methodologies can be found in [8], [9], [10], and [11], for breast lesion detection. Furthermore, a comprehensive prototype has been presented in [12] for 3D microwave brain stroke imaging, with validated experimental results on fabricated phantoms.

Besides these prototypes, a novel device (MammoWave, UBT Srl, Italy) has been introduced for breast lesion detection [13]. MammoWave is uniquely skilled to work with two antennas spinning in the azimuth plane, operating within the microwave band.

MammoWave uses a Huygens principle (HP) based imaging algorithm, first introduced in [14]. HP-based imaging algorithm makes computational burden very low, as there is no need to solve the inverse problem and matrix generation or inversion, making it an appropriate technique for medical microwave imaging. This methodology helps to gather all the information from individual frequencies in the frequency domain to reconstruct a consistent image [14]. MammoWave capability in breast lesion detection has been verified clinically [15]; in addition, the device has also been adapted to perform phantom imaging for brain stroke and bone lesions detection [16], [17]. All MammoWave images are evaluated in 2D and at one plane along the z-axis, after removing the artefacts [18].

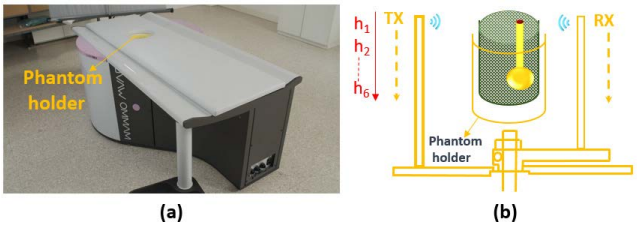

FIGURE 1. (a) MammoWave microwave imaging device having a cylindrical hub and the phantom holder, designed by UBT, (b) Experimental schematic i.e., fabricated phantom inside phantom holder with changing heights of antennas for multiple cross-sectional analysis along the z-axis.

In this paper, the MammoWave device (shown in Fig.1(a)) has been exploited for the extension of the imaging algorithm from 2D to 3D by performing a multi-plane scanning experiment. For this purpose, a cylindrical fabricated phantom having a 3D structured tube as an inclusion (mimicking a lesion) has been used for experimentation. Measurements have been acquired in multiple planes along the z-axis. The inclusion has been successfully detected in multiple planes by implementing a modified HP based algorithm via superimposition theorem. Image processing and adjustment has been applied to the reconstructed images for 3D visualization and discovering the dimensions of inclusion at multiple planes. Next, to evaluate our proposed 3D imaging algorithm's capability in a more realistic scenario, we have repeated the measurements employing a skull-mimicking phantom having an inclusion.

In [19] some preliminary results have been presented without any quantification, while in this paper 3D imaging performances have been quantified and validated by calculating S/C ratio and dimensional error. Moreover, we have quantified performance degradation when modifying imaging parameters. We have also included measurements performed using a 3D skull shaped head phantom. Finally, we have included a comprehensive localization error quantification.

II. EXPERIMENTAL CONFIGURATION

A. DEVICE & METHODOLOGY

In this paper, all the results and images have been acquired by exploiting MammoWave. The device has a cylindrical hub made of aluminium and is equipped with internal microwave absorbers. The device comprises two antennas, Tx (transmitter) and the Rx (receiver) operating here in the frequency range of 1 to 6.5 GHz. Tx and Rx antennas rotate in a circular direction in the azimuth plane in free space. Antennas are connected to a vector network analyzer (Cobalt C1209, Copper Mountain, Indianapolis, IN) and are installed at the same height.

Both antennas are rotatable and cover 360°. Tx plane is divided into 5 angular sections with a difference of 72°,i.e., transmitting the signals from 5 central points (0°, 72°, 144°, 216°, 288°). Besides these central points, in each triplet the Tx transmits the signals from two other angularly displaced positions by ±4.5° rotation with respect

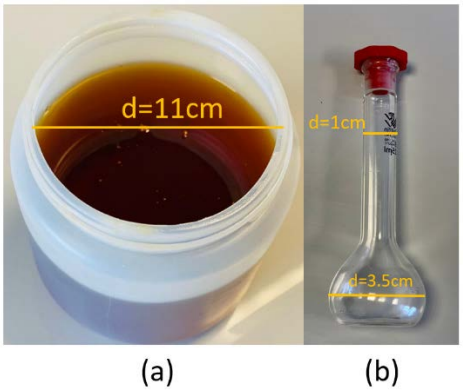

FIGURE 2. (a) Fabricated phantom, (b) 3D structured inclusion.

TABLE 1. Relative permittivity and conductivity of fabricated materials at 2 GHz [18], [20].

Fabrication Material	Relative Permittivity (ε_r)	Conductivity (σ) [S/m]
ZMT Zürich MedTech, Swiss, TLe11.5c.045oil	7	0.3
40% glycerol and 60%water	60	2

to the central points, resulting in a total of 15 transmitting positions. The receiver antenna can receive the signals every 4.5°, which will lead to 80 receiving points [13].

Furthermore, the device comprises of cylindrically shaped phantom holder, Tx and Rx antennas rotate around the phantom holder in circular direction. The device has been used in [13], [15], [16], and [17] with the measurements being taken only in one plane along the z-axis, producing 2D results. This paper presents a novel methodology of applying MWI at different planes/heights along the z-axis. Superimposition theorem has been employed on the measurements taken at different planes alongside the z-axis by taking one reference plane and then moving downwards along the z-axis with equal distances between each successive two planes. The experimental methodology is shown in Fig. 1b; measurements at different planes have been taken by changing the height of both antennas (Tx & Rx) using a GUI designed for operating the MammoWave device. As both antennas remain at the same height, the change in height is carried out simultaneously for both antennas.

B. PHANTOM FABRICATION

A cylindrically shaped plastic container has been used as a phantom with a diameter of 11 cm and a height of 13 cm. The inclusion employed in our first measurement is a 3D-shaped tube with a spherical bottom, the diameter of the tube at its upper part (7.5 cm in length) is 1 cm, which increases gradually to 3.5 cm at its lower part as shown in Fig. 2(b). The purpose of using 3D structured inclusion is to validate the 3D imaging algorithm by detecting the dimension of inclusion at multiple planes.

FIGURE 3. Fabricated head phantom.

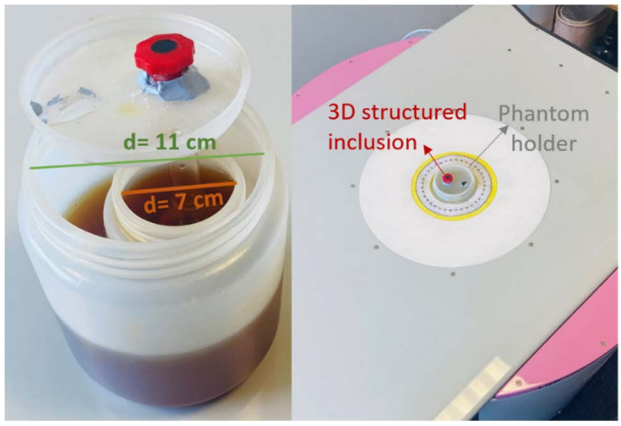

FIGURE 4. Fabricated 3-layer phantom (left), and the experimental setup (right).

The main concept of MWI is to exploit the contrast in dielectric properties, i.e., relative permittivity and conductivity, between healthy tissues and tissues having lesions (such as tumors). The material used to fabricate the cylindrical phantom is TLe11.5c.045 oil by ZMT Zürich MedTech, Swiss, a mixture of 40% glycerol and 60% water has been used for the inclusion mimicking the lesion.

The materials used to fabricate the phantom and inclusion are prepared by considering dielectric property differences and the stability of the materials. The dielectric properties of both materials at a frequency of 2 GHz are presented in Table 1 [18], [20].

In order to validate the ability of 3D imaging algorithm we have fabricated a skull-mimicking phantom with the axis dimension of 7 cm × 10 cm × 15.5 cm, having a cylindrically shaped tube as an inclusion with radius of 0.7 cm as shown in Fig. 3.

The skull-mimicking phantom has been filled with oil; the bottom 1 cm of the tube has been filled with water, while the remaining part of the tube has been filled with the same oil used in the skull. Dielectric properties of the oil used may be found in [17].

Another more complex scenario has been considered to show further validation of the proposed 3D imaging algorithm through addition of an internal cylindrical layer with a diameter of 7 cm to the first experimental setup, as shown

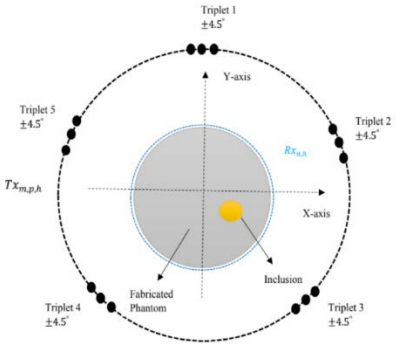

FIGURE 5. Pictorial view of the measurement process, where grey coloured circle represents the fabricated phantom, light blue dots indicate the receiving points, small yellow circle shows the inclusion. The outer dashed black circle shows the transmitting antenna perimeter with dark circles in sets of three showing the transmitter triplets.

in Fig. 4. This internal cylindrical phantom has been placed eccentrically with an offset of 3.5 cm and filled with TLe5c24 liquid oil having $\varepsilon = 5$ and $\sigma = 0.2$. We have used the same 3D structured spherical inclusion as the first experiment, however for this scenario only the spherical part of the inclusion (positioned inside the internal layer) has been filled with the fabrication mixture.

III. IMAGING PROCEDURE

In MammoWave, both antennas have been programmed to rotate in an azimuth plane in free space around the object under experimentation. HP states that every point on the wave front of the wave is a source of secondary wavelet with the same information as the original without any loss and so on; the resultant will be the envelope to those wavelets. In this paper, the HP is applied to the measurements taken on different planes and the measurements are then processed into images based on the difference in dielectric properties of the materials, mimicking the contrast between tumor and healthy tissues.

Rx antenna can rotate ±4.5° to receive the transmitted signals at receiving points, which can be stated as $\mathrm{Rx}_{n,h} \equiv (a_0, \emptyset_n, Z_h) \equiv \overrightarrow{\rho_{n,h}}$ in the circular direction having radius a_0 at multiple planes alongside the z-axis. The received signal at multiple planes Z_h along the z-axis at different heights h can be represented as S21:

$$\mathrm{S21}_{n,h}^{m,p}\left(a_0, \emptyset_n, Z_h; \mathrm{Tx}_{m,p,h}; f\right) \tag{1}$$

where $n = 1, 2, \ldots, 80$ indicates the receiving points; $m = 1, 2, \ldots, 5$ specifies the central transmitting positions, $p = 1, 2, 3$ indicates the positions inside transmitting sections with the angular displacement of ±4.5°, f is the frequency, Z_h represents the multiple planes along the z-axis and $h = 1, 2, \ldots, H$, is the number of heights along the z-axis (variable heights, i.e. H can be changed as per requirements). Fig. 5 shows the pictorial view of the measurement process with the phantom and inclusion.

The measured received signal ($E_{\mathrm{i}\mathrm{Tx}_{m,p,h}}^{\mathrm{known}}|_{Rx_{n,p,h}} = \mathrm{E}_{\mathrm{i}_{\mathrm{n,Tx}_{\mathrm{m,p,h}}}}^{\mathrm{known}}$ on multiple planes Z_h) is then processed using HP to evaluate the field inside the cylinder. The measured external field carries the information of dielectric contrast of the mixtures inside the fabricated phantom for NPT observing points at multiple heights h_n, which can be represented as the reconstructed field:

$$E_{\mathrm{HP,3D}}^{\mathrm{rcstr}}\left(\rho, \emptyset, Z; \mathrm{Tx}_{m,p,h}; f\right) = \sum_{h=1}^{h_n}\sum_{n=1}^{NPT} S21_{n,h}^{m,p}\left(a_0, \emptyset_n, Z_h; \mathrm{Tx}_{m,p,h}; f\right) G\left(k_1\left|\overrightarrow{\rho_{n,h}} - \vec{\rho}\right|\right) \tag{2}$$

In Eq. 2 'rcstr' indicates the reconstructed internal field, 'HP' indicates the procedure used to measure the reconstructed field and '3D' indicates the employment of the superimposition theorem for 3D visualization of the inclusion.

Moreover, $\rho = (\rho, \emptyset, Z)$ and $\overrightarrow{\rho_{n,h}} = (a_0, \emptyset_n, Z_h)$ in Eq. (2) are the observation points at multiple planes Z_h. k_1 indicates the wavenumber, which is set here to be the free space dielectric constant. Green's function G, as implemented in Eq. 3 has been used to propagate the field for multiple planes alongside the z-axis.

$$G\left(k_1\left|\overrightarrow{\rho_{n,h}} - \vec{\rho}\right|\right) = \frac{1}{4\pi\left|\overrightarrow{\rho_{n,h}} - \vec{\rho}\right|} e^{-jk_1\left|\overrightarrow{\rho_{n,h}} - \vec{\rho}\right|} \tag{3}$$

Furthermore, the Green's function implies a singularity for $\left|\overrightarrow{\rho_{n,h}} - \vec{\rho}\right| = 0$; however, this singularity may be cancelled by multiplying the Green's function by $\left|\overrightarrow{\rho_{n,h}} - \vec{\rho}\right|$ as pointed out in [14]. $E_{\mathrm{HP,3D}}^{\mathrm{rcstr}}$ is calculated separately for Z_h and does not calculate the accurate field but rather captures the dielectric contrast between the inclusion and the surrounding material, enough for locating the target. It has to be highlighted that we are not interested in evaluating the internal field; instead, our aim is to capture the contrast (mismatched boundaries) and locating the inclusion within the volume [14], [22].

Assume we use N_F frequencies f_i in the frequency band B at multiple planes h_n, intensity I of the image can be obtained by incoherently summing all the solutions.

$$I_{\mathrm{3D}}\left(\rho, \emptyset, Z; Tx_{m,p,h}\right) = \sum_{h=1}^{h_n}\sum_{i=1}^{NF}\left|E_{\mathrm{HP}}^{\mathrm{rcstr}}(\rho, \emptyset, Z; \mathrm{Tx}_{m,p,h}; f_i)\right|^2 \tag{4}$$

Artefacts can be removed by subtracting between S21 obtained using two measurements at different positions in the triplet such as $p = 1,2,3$ and $\acute{p} = 1,2,3$, with $p \neq \acute{p}$ for multiple planes as shown in Eq. 5.

$$E_{\mathrm{HP,3D}}^{\mathrm{rcstr}}\left(\rho, \emptyset, Z; \mathrm{Tx}_{m,p,h} - \mathrm{Tx}_{m,\acute{p},h}; f\right) = \sum_{h=1}^{h_n}\sum_{n=1}^{NPT}\begin{pmatrix} \mathrm{S21}_{n,h}^{m,p}\left(a_0, \emptyset_n, Z_h; \mathrm{Tx}_{m,p,h}; f\right) \\ -\mathrm{S21}_{n,h}^{m,\acute{p}}\left(a_0, \emptyset_n, Z_h; \mathrm{Tx}_{m,\acute{p},h}; f\right)\end{pmatrix} \tag{5}$$

The images of the sections are then summed up to get the final image at multiple heights along the z-axis as follows

in Eq. 6:

$$I_{3D}(\rho, \emptyset, Z) = \sum_{h=1}^{6}\sum_{m=1}^{5}\sum_{\substack{p=1 \\ \acute{p}=1 \\ \acute{p}\neq p}}^{3}\left(I\left(\rho, \emptyset, Z; \mathrm{Tx}_{m,p,h} - \mathrm{Tx}_{m,\acute{p},h}; f_i\right)\right)^2 = \sum_{h=1}^{6}\sum_{m=1}^{5}\sum_{\substack{p=1 \\ \acute{p}=1 \\ \acute{p}\neq p}}^{3}\sum_{i=1}^{NF}\left|E_{\mathrm{HP}}^{\mathrm{rcstr}}(\rho, \emptyset, Z; \mathrm{Tx}_{m,p,h}; f_i)\right|^2 \quad (6)$$

The procedure we use follows a theoretical justification, as described in [22]; the proposed procedure can be seen as an application of holography theory which was first developed by R. P. Porter and A. J. Devaney in the early 1980s [23], [24]. The proposed methodology indicated that an inverse source problem could be determined from the value of the field and its normal derivative over any closed surface surrounding the volume of interest. However, [23], [24] are focused on recuperating the map of the dielectric properties in the volume, recognizing the contrast in dielectric properties. Contrariwise, the approach proposed here solves a simpler computational problem by seeking only to identify the significant scatterers; to achieve our goal, only the field on an arbitrary closed surface is used.

The proposed HP-based imaging algorithm is different from the Kirchhoff migration algorithm, which usually performs back-propagation and time reversal to solve the inverse problems and finding the phase, i.e., time, trace. [6]. The key features of HP based algorithm involves capturing the dielectric contrast during the reconstruction process without finding the phase and performing a non-coherent summation in the frequency domain. Therefore, the proposed methodology allows us to gather the information from individual frequencies, which plays a crucial role in reconstructing a consistent image [14].

IV. RESULTS AND DISCUSSION

Overall, six measurements have been performed for each phantom, at multiple planes Z_h along the z-axis. For each measurement, considering 15 transmitting positions (5 triplets) and 80 receiving points in the frequency range of 1-6.5 GHz, we generate a 1200×1101 raw data matrix of S21 complex values. In our antenna's measurement setup, we only use the copolar component of the field, which is, in this case, vertically polarized. We have shown in our initial works [14] that this component is enough for detection of the mismatch even though it does not reconstruct the exact internal field.

For each measurement i.e., multiple planes, the radius is the same $a_0 = 0.07$ m and the measurement process at each plane takes approximately 9-10 minutes. Then the raw data is processed through HP taking around 4-5 minutes to process the data from all planes at the same time. The measurement

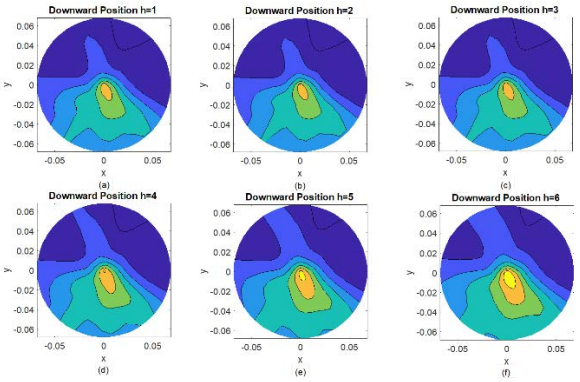

FIGURE 6. Microwave images with detected inclusion at reference planes: (a) $h = 1$, (b) $h = 2$, (c) $h = 3$, (d) $h = 4$, (e) $h = 5$, (f) $h = 6$. Axes units are meters.

time corresponds to performing measurement with 80 receiving positions and 5 MHz frequency sampling. However, the time can be noticeably reduced by decreasing the number of points or increasing the frequency step. More specifically, in our previous works [14], [25], we have shown on phantoms that the number of receiving points can be reduced to a spatial sampling of lambda/2, where lambda is the wavelength in the phantom calculated at the maximum measured frequency, leading to 24 receiving points in [14], without a significant drop in signal to clutter ratio. In the same paper, we have also shown that the frequency sampling may be increased to 20MHz. As the phantom used in [25] was a multilayer lousy gel phantom having similar properties to human tissues we may assume that the time reduction can still achieve good detection and localization in real scenarios.

Raw data for all 6 planes along the z-axis have been processed simultaneously and are dealt with in the same coordinates when applying the superimposition theorem in the modified HP-based 3D imaging algorithm. Obtained images have been gathered in Fig. 6, which shows the detected inclusion at multiple planes along the z-axis. The images have been obtained after removing the artefacts by subtracting the S21 at different positions with respect to the transmitting positions (specifically, a 9° displacement has been used in the images presented here) at each plane.

Fig. 6(a) shows the inclusion detected at a reference position starting from the top $h = 1$, Fig. 6(b) shows the inclusion detected at $h = 2$ (downward direction along the z-axis), Fig. 6(c) shows the inclusion detected at $h = 3$ (downward direction along the z-axis) and so on till $h = 6$. The results presented in Fig. 6 clearly show that the size of the detected inclusion varies while taking measurements at multiple planes.

Furthermore, the results have been plotted by separating each plane along the z-axis to visualize the dimensional analysis of the detected inclusion and comparing with realistic parameters.

All the images at multiple planes have been generated on the same coordinates, and Figs. 6(d), 6(e), and 6(f) indicate

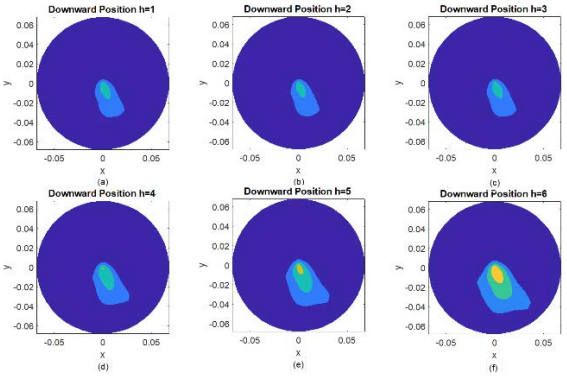

FIGURE 7. Normalized and adjusted microwave images with highlighted inclusion at reference planes: (a) $h = 1$, (b) $h = 2$, (c) $h = 3$, (d) $h = 4$, (e) $h = 5$, (f) $h = 6$. Axes units are meters.

that the size of the detected inclusion increases while going downwards at different planes. This increase in the size of the inclusion indicates the successful implementation of the superimposition theorem and validates the 3D visualization of the inclusion at multiple planes by plotting the planes separately.

The images obtained are again processed using an image processing toolbox in MATLAB by adjusting the images and highlighting the detected inclusion in order to clearly show the varying size of the inclusion at multiple planes. A threshold value of 0.5 is chosen here to remove the clutter without affecting the target detection. Fig. 7 shows the highlighted detected inclusion after processing the obtained images in Fig. 6 and highlighting the perceived inclusion by removing the artefacts and normalizing to the global maximum value.

In Fig. 7 the size of the inclusion varies and becomes larger while going downwards along the z-axis, with the size of the spotted inclusion agreeing with the actual inclusion size at different heights. These results unambiguously reveal the successful repercussion of the superimposition theorem and 3D visualization.

The applied image adjustment is performed by applying threshold to the intensity value in order to provide a better 3D visualization, without changing the information content that could affect target detection and localization. For example, looking at Figs. 6 and 7, correct detection and localization can be observed in both sets of figures, while they vary in terms of visualization. Therefore, the applied adjustment does not affect image reconstruction but affects the visualization by highlighting the inclusion for observing varying dimensions and detections on the multiple planes along the z-axis.

Fig. 8 depicts the 3D visualization of the detected inclusion with reference to the cross-sections along the z-axis before and after normalization and adjustment, respectively. It shows the detected inclusion at all the planes along the z-axis where measurements had been taken and clearly indicates the resemblance in dimensions of the detected inclusion with the realistic inclusion. The obtained results effectively authenticate the potential of HP-based 3D imaging algorithm

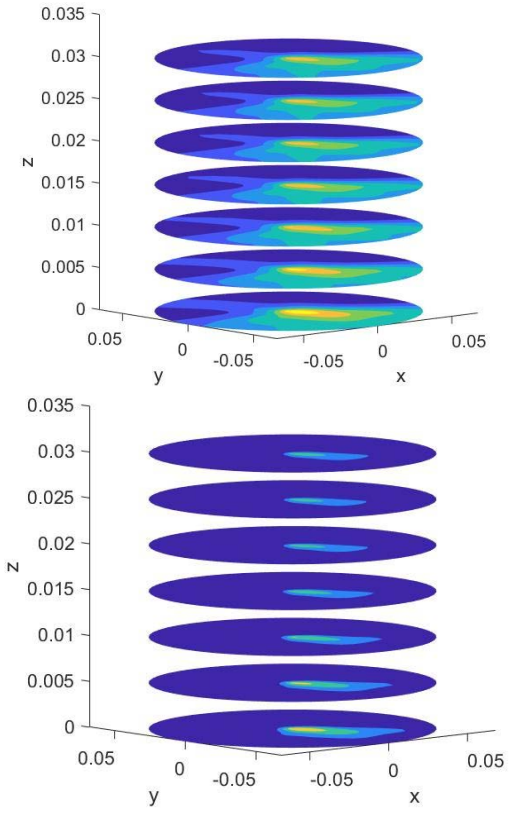

FIGURE 8. 3D Visualization of the detected inclusion in multiple cross-sections along the z-axis, before (above) and after (below) normalization and adjusting. Axes units are meters.

to detect the dimension of inclusion and reconstruction of the 3D image via superimposition theorem.

We have quantified the results obtained by validating the signal to clutter ratio and dimensional analysis of the inclusion at multiple planes. The signal to clutter (S/C) ratio is defined as the ratio between the maximum intensity calculated within the region of inclusion and maximum intensity outside the region of the inclusion [21]. The S/C ratio has been calculated at each plane along the z-axis and is presented in Table 2, which clearly indicates that the inclusion has been successfully detected along z-axis dimensions.

The dimensional analysis is the comparison between the realistic parameters and the detected inclusion's parameters. The inclusion used in this study is 3D structured and possesses different dimensions at different cross-sections along the z-axis.

In Table 3, dimensions of the detected inclusion at multiple planes have been measured in terms of the diameter (average) and compared with the realistic parameters along with the calculated error percentage. Image quantification illustrates the successful implementation of a 3D HP-based imaging algorithm, demonstrating a S/C ratio ranging from 7 to 10 dB and a detection of the dimensions of the inclusion with an error lower than 7.5%.

In order to confirm the ability of the 3D HP-based imaging algorithm to localize the inclusion, we have developed the

TABLE 2. Signal to clutter at multiple planes along the z-axis.

Z_h along the z − axis	Planes / Cross-sections	Signal to Clutter ratio (S/C) [dB]
Reference plane	h=1	7.88
0.5 cm Downward	h=2	7.94
1 cm Downward	h=3	7.92
1.5 cm Downward	h=4	10.52
2 cm Downward	h=5	10.59
2.5 cm Downward	h=6	10.54

TABLE 3. Dimensional analysis and error % calculations at multiple planes.

Z_h / Cross-sections	*Diameter of Fabricated Inclusion [cm]*	*Diameter (average) of detected Inclusion [cm]*	*Error Percentage [%]*
h=1	1	1.02	2
h=2	1	1.07	7
h=3	2.2	2.04	7.27
h=4	2.6	2.5	3.8
h=5	3	2.9	3.3
h=6	3.5	3.7	5.71

following methodology to further validate our results. Corresponding to the images shown in Figs. 6 and 7, for comparison purposes we have considered the results obtained at heights i.e., $h = 2$, 4, and 6, shown in Fig. 9, with a red circle indicating the true position and dimension of the inclusion at each height.

The HP based imaging algorithm requires the information on dielectric properties of the outside medium (here free space) to achieve detection, Figs. 6-9 show the reconstructed images using free space dielectric properties. The main idea is to provide altered information of dielectric properties to the 3D HP-based imaging algorithm to observe the changes in the detection and localization of the detected inclusion and assess the robustness of the HP algorithm. Therefore, we have performed two studies with altered permittivity and conductivity information, given as input to the algorithm.

After processing the data with the changed parameters provided to the HP-based imaging algorithm, we can still successfully detect the inclusion, which indicates the robustness of the HP algorithm with respect to the errors in the knowledge of the dielectric properties.

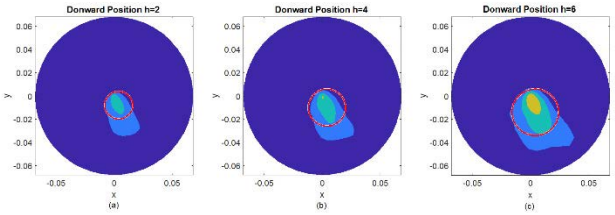

FIGURE 9. Microwave images with detected inclusion (circled) at $h = 2$, 4 and 6. Axes units are meters.

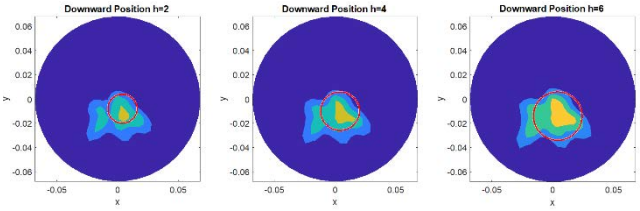

FIGURE 10. Normalized and adjusted Microwave images with detected inclusion (permittivity increased by a factor of 4) at $h = 2$, 4 and 6. Axes units are meters.

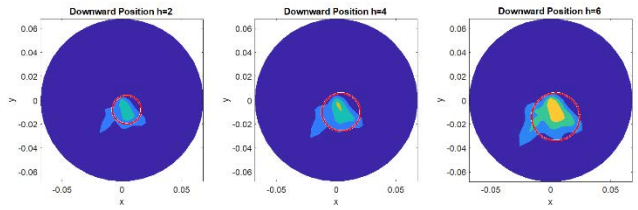

FIGURE 11. Normalized and adjusted Microwave images with detected inclusion (permittivity and conductivity increased by factors of 4 and 2, respectively) at $h = 2$, 4 and 6. Axes units are meters.

The position of the inclusion has been slightly displaced from the original, as there is a very slight offset and decreased dimension accuracy. We have made changes to all 6 planes along the z-axis as our modified algorithm allows us to process multiple planes at a time, for visualization we have highlighted only planes 2, 4, and 6 along the z-axis. As the circled parts in Figs. 10 and 11 show, the actual position of the inclusion is slightly displaced compared with the detected.

We have also quantified the results obtained in Figs. 9 and 10 by calculating the S/C ratio at each plane along the z-axis, which is shown in Table 4 for both scenarios. As we can observe, the localization of the inclusion is successfully achieved; however, the S/C ratio drops compared to the results in Table 2.

The dimensional analysis error of the detected inclusion increases from 7.5% to 18% when increasing the permittivity and 24% when increasing both permittivity and conductivity. Nevertheless, we still have detection and localization of the inclusion despite the inaccurate information provided to the algorithm.

Furthermore, in order to validate the effect of dielectric properties in localization we have calculated the localization error i.e., the distance between the actual center of the inclusion and centroid of the detected inclusion in the normalized

TABLE 4. Signal to clutter comparison with increased values of ε & σ at multiple planes along the z-axis.

Z_h along the z − axis	S/C [dB] ε_r =4	S/C [dB] ε_r =4, σ=0.2 [S/m]
Reference plane, h=1	1.12	2.78
0.5 cm Downward, h=2	1.21	2.99
1 cm Downward, h=3	2.74	2.93
1.5 cm Downward, h=4	2.72	3.50
2 cm Downward, h=5	4.16	3.91
2.5cm Downward, h=6	5.87	4.19

TABLE 5. Localization error comparison between free space parameters and increased values of ε & σ at multiple planes along the z-axis.

Z_h	Localization error (mm) Free space parameters	Localization error (mm) ε_r =4	Localization error (mm) ε_r =4, σ=0.2
h=2	3.42	3.81	4.03
h=4	5.82	7.66	7.78
h=6	7.57	10.57	10.65

and adjusted image, both before and after changing the dielectric properties as shown in Table 5. In order to calculate the centroid, we have created the binary version of the adjusted reconstruction image through thresholding.

It can be perceived that the localization error increases when changing the parameters. From Table 5 and images in Figs. 9 and 10 we can conclude that, while the detection results satisfy our aim of validating the robustness of the imaging algorithm with respect to the knowledge of the dielectric property, we experience an increase in localization error.

Corresponding to the skull-mimicking phantom, the same measurement procedure was followed (six measurements at multiple planes along the z-axis) starting from top of the skull phantom and going downwards. For this measurement, we have fabricated the inclusion with uniform cross-section (i.e. cylindrical) but with varying dielectric properties along the z-axis. Specifically, the bottom 1 cm of the tube was filled with water and the remaining with the same oil used in skull. This reflects a 3D variation in terms of dielectric properties along the z-axis.

Figs. 12 and 13 show the reconstructed images from the experimental data utilizing the proposed HP based 3D imaging algorithm before and after normalization and adjustment, respectively. The obtained images show the highest S/C ratio (9 dB) at plane 6, which is the cross-sectional analysis of the plane possessing the portion filled with 1 cm of water

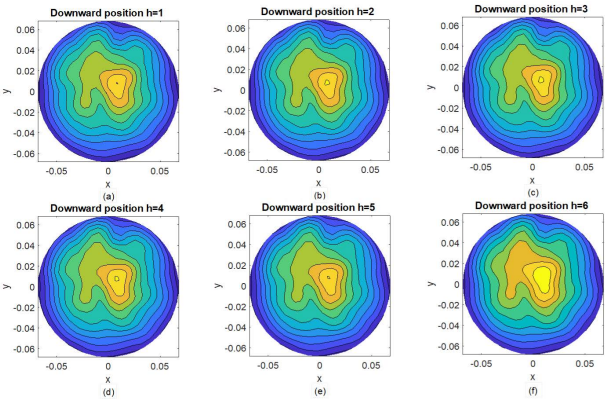

FIGURE 12. Microwave images with detected inclusion at reference planes (head-phantom): (a) h = 1, (b) h = 2, (c) h = 3, (d) h = 4, (e) h = 5, (f) h = 6. Axes units are meters.

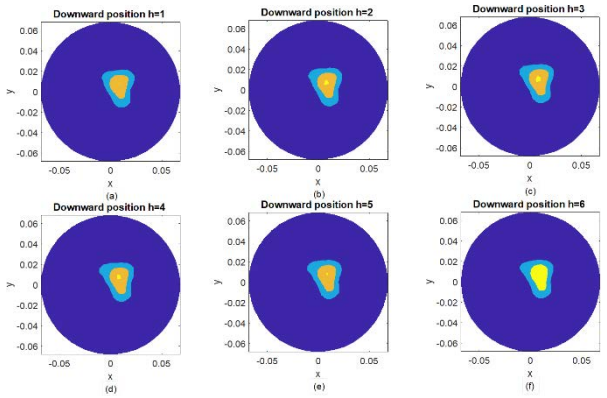

FIGURE 13. Normalized and adjusted microwave images with detected inclusion at reference planes (head-phantom): (a) h = 1, (b) h = 2, (c) h = 3, (d) h = 4, (e) h = 5, (f) h = 6. Axes units are meters.

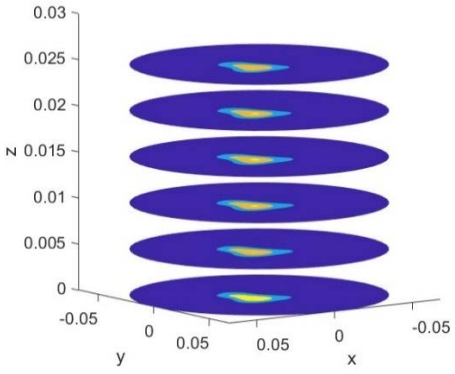

FIGURE 14. 3D Visualization of the detected inclusion in multiple cross-sections along the z-axis (head-phantom) after normalization and image adjusting. Axes units are meters.

(mimicking inclusion). Fig. 14 shows the successful 3D visualization of the reconstructed images after normalizing and image adjusting.

The same experimental methodology has been applied for the 3-layer cylindrical phantom. We have performed measurements at six multiple planes along the z-axis by changing

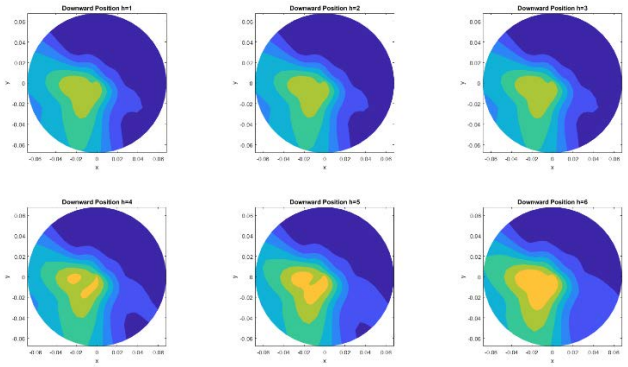

FIGURE 15. Microwave images with detected inclusion at reference planes (3-layer phantom): (a) $h = 1$, (b) $h = 2$, (c) $h = 3$, (d) $h = 4$, (e) $h = 5$, (f) $h = 6$. Axes units are meters.

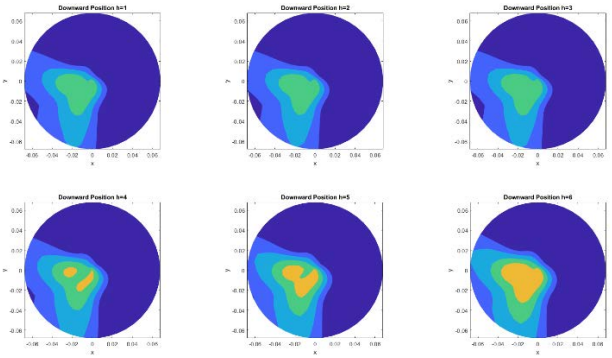

FIGURE 16. Normalized and adjusted microwave images with detected inclusion at reference planes (3-layer phantom): (a) $h = 1$, (b) $h = 2$, (c) $h = 3$, (d) $h = 4$, (e) $h = 5$, (f) $h = 6$. Axes units are meters.

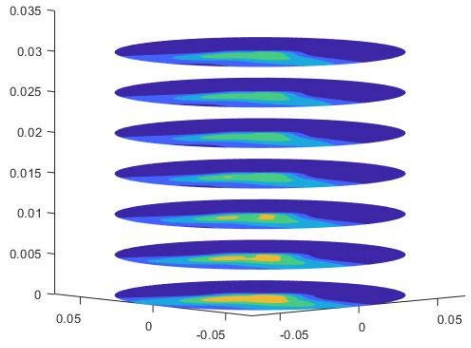

FIGURE 17. 3D Visualization of the detected inclusion in multiple cross-sections along the z-axis (3-layer phantom) after normalization and image adjusting. Axes units are meters.

the height of the antennas simultaneously (similar to previous experiments). Figs. 15 and 16 show the images reconstructed for six planes along the z-axis before and after image normalization and adjustment respectively.

In this experiment, only the spherical part of the inclusion was filled with the inclusion fabrication mixture, and we aimed that to reflect in our reconstructed images. Figs. 15 and 16 clearly show the successful detection of the spherical cross-sectional analysis which can be seen most prominently at h = 6 along the z-axis (with highest S/C ratio of 10.48dB), given it is the height with the largest diameter.

The results in Figs. 15 and 16 show the successful implementation of superimposition theorem and validate the capability of HP based imaging algorithm in multi-layered complex scenarios. Furthermore, the dimensional analysis error, as compared with the realistic setup, is less than 6% at h = 6, which is slightly higher than the corresponding error of the same height in the first experiment, reported in Table 3. This clearly indicates the successful implementation of the 3D HP based imaging algorithm.

Hence, the Fig. 17 shows the 3D visualization of the reconstructed images after image normalization and adjustment at multiple slices along the z-axis.

V. CONCLUSION

In this paper, a new 3D imaging algorithm based on the Huygens principle was presented and validated by measurements on three fabricated phantoms. The received complex signals S21 using 5 transmitting positions in the form of triplets and 80 receiving points for Z_h planes along the z-axis have been processed and validated by implementing a new 3D imaging algorithm. A 3D structured inclusion (tube with spherical bottom) was initially used, and the measurements were performed on different planes alongside the z-axis. The measurements were taken using the MammoWave MWI device; this device is completely safe as it does not use ionizing radiations. MammoWave is operated by a designed GUI, automating the change in the position of the antennas, which facilitated the taking of measurements on different planes along the z-axis. The main purpose of this investigation was to visualize the detected inclusion in 3D, and to accomplish this task a superimposition theorem was employed by gathering the results from multiple planes Z_h and visualizing them in 3D by superimposing the results i.e., one plane on another. The results obtained validate the proposed procedure, as the detected inclusion's size varies in accordance with the realistic inclusion with an error $<7.5\%$. Subsequently, a skull shape phantom containing a cylindrically shaped inclusion was also used and the measurements were repeated on different planes alongside the z-axis. For skull shaped head phantom, the target detection is more prominent on the last plane along z-axis, which agrees with our setup, thus validating the successful implication of our algorithm. Finally, we have further validated our proposed 3D imaging algorithm in more complex scenario i.e., fabricating a 3-layer phantom with different dielectric properties and employing a 3D structured spherical inclusion.

REFERENCES

[1] R. Chandra, H. Zhou, I. R. M. B. Narayanan, P. M. de Azevedo-Marques, A. Mencattini, M. Salmeri, and R. M. Rangayyan, "Medical microwave imaging and analysis," in *Medical Image Analysis and Informatics: Computer-Aided Diagnosis and Therapy*. Boca Raton, FL, USA: CRC Press, 2018, pp. 451–466.

[2] S. Semenov, "Microwave tomography: Review of the progress towards clinical applications," *Philos. Trans. Roy. Soc. A, Math., Phys. Eng. Sci.*, vol. 367, pp. 3021–3042, Aug. 2009.

[3] M. S. Goyal and V. S. Kushwah, "Study of UWB wireless communication for recent medical applications," in *For Healthcare Professionals: Scope and Opportunities*. Gwalior, India: Amity Univ. Madhya Pradesh, Amity Institute of Pharmacy, 2020, p. 144.

[4] B. Allen, A. Brown, K. Schwieger, E. Zimmermann, W. Q. Malik, D. J. Edwards, and L. Ouvry, "Ultra-wideband: Applications, technology, and future perspectives," in *Proc. Int. Workshop Convergent Technol. (IWCT)*, 2005.

[5] E. J. Bond, X. Li, S. C. Hagness, and B. D. Van Veen, "Microwave imaging via space-time beamforming for early detection of breast cancer," *IEEE Trans. Antennas Propag.*, vol. 51, no. 8, pp. 1690–1705, Aug. 2003.

[6] M. A. Elahi, B. R. Lavoie, E. Porter, M. Olavini, E. Jones, E. C. Fear, and M. O'Halloran, "Comparison of radar-based microwave imaging algorithms applied to experimental breast phantoms," in *Proc. 32nd Gen. Assem. Sci. Symp. Int. Union Radio Sci. (URSI GASS)*, Aug. 2017, pp. 1–4.

[7] N. K. Nikolova, "Microwave imaging for breast cancer," *IEEE Microw. Mag.*, vol. 12, no. 7, pp. 78–94, Dec. 2011.

[8] A. W. Preece, I. J. Craddock, M. Shere, L. Jones, and H. L. Winton, "MARIA M4: Clinical evaluation of a prototype ultrawideband radar scanner for breast cancer detection," *J. Med. Imag.*, vol. 3, no. 3, 2016, Art. no. 033502.

[9] M. Guardiola, S. Capdevila, J. Romeu, and L. Jofre, "3-D microwave magnitude combined tomography for breast cancer detection using realistic breast models," *IEEE Antennas Wireless Propag. Lett.*, vol. 11, pp. 1622–1625, 2012.

[10] T. M. Grzegorczyk, P. M. Meaney, P. A. Kaufman, R. M. Diflorio-Alexander, and K. D. Paulsen, "Fast 3-D tomographic microwave imaging for breast cancer detection," *IEEE Trans. Med. Imag.*, vol. 31, no. 8, pp. 1584–1592, Aug. 2012.

[11] M. T. Bevacqua and R. Scapaticci, "A compressive sensing approach for 3D breast cancer microwave imaging with magnetic nanoparticles as contrast agent," *IEEE Trans. Med. Imag.*, vol. 35, no. 2, pp. 665–673, Feb. 2016.

[12] J. A. Tobon Vasquez, R. Scapaticci, G. Turvani, G. Bellizzi, D. O. Rodriguez-Duarte, N. Joachimowicz, B. Duchêne, E. Tedeschi, M. R. Casu, L. Crocco, and F. Vipiana, "A prototype microwave system for 3D brain stroke imaging," *Sensors*, vol. 20, no. 9, p. 2607, May 2020.

[13] A. Vispa, L. Sani, M. Paoli, A. Bigotti, G. Raspa, N. Ghavami, S. Caschera, M. Ghavami, M. Duranti, and G. Tiberi, "UWB device for breast microwave imaging: Phantom and clinical validations," *Measurement*, vol. 146, pp. 582–589, Nov. 2019.

[14] N. Ghavami, G. Tiberi, D. J. Edwards, and A. Monorchio, "UWB microwave imaging of objects with canonical shape," *IEEE Trans. Antennas Propag.*, vol. 60, no. 1, pp. 231–239, Jan. 2012.

[15] L. Sani, A. Vispa, R. Loretoni, M. Duranti, N. Ghavami, D. A. Sánchez-Bayuela, S. Caschera, M. Paoli, A. Bigotti, M. Badia, M. Scorsipa, G. Raspa, M. Ghavami, and G. Tiberi, "Breast lesion detection through MammoWave device: Empirical detection capability assessment of microwave images' parameters," *PLoS ONE*, vol. 16, no. 4, Apr. 2021, Art. no. e0250005.

[16] B. Sohani, J. Puttock, B. Khalesi, N. Ghavami, M. Ghavami, S. Dudley, and G. Tiberi, "Developing artefact removal algorithms to process data from a microwave imaging device for haemorrhagic stroke detection," *Sensors*, vol. 20, no. 19, p. 5545, Sep. 2020. [Online]. Available: https://www.mdpi.com/1424-8220/20/19/5545

[17] B. Khalesi, B. Sohani, N. Ghavami, M. Ghavami, S. Dudley, and G. Tiberi, "Free-space operating microwave imaging device for bone lesion detection: A phantom investigation," *IEEE Antennas Wireless Propag. Lett.*, vol. 19, no. 12, pp. 2393–2397, Dec. 2020, doi: 10.1109/LAWP.2020.3034039.

[18] J. Puttock, B. Sohani, B. Khalesi, G. Tiberi, S. Dudley-McEvoy, and M. Ghavami, "UWB microwave imaging for inclusions detection: Methodology for comparing artefact removal algorithms," in *Proc. EAI Int. Conf. Body Area Netw.* Cham, Switzerland: Springer, Oct. 2020, pp. 46–58.

[19] B. Khalid, B. Khalesi, N. Ghavami, S. Dudley, M. Ghavami, and G. Tiberi, "3D microwave imaging using Huygens principle: A phantom-based validation," in *Proc. Photon. Electromagn. Res. Symp. (PIERS)*, Nov. 2021, pp. 2892–2896.

[20] P. M. Meaney, C. J. Fox, S. D. Geimer, and K. D. Paulsen, "Electrical characterization of glycerin: Water mixtures: Implications for use as a coupling medium in microwave tomography," *IEEE Trans. Microw. Theory Techn.*, vol. 65, no. 5, pp. 1471–1478, May 2017.

[21] E. C. Fear, X. Li, S. C. Hagness, and M. A. Stuchly, "Confocal microwave imaging for breast cancer detection: Localization of tumors in three dimensions," *IEEE Trans. Biomed. Eng.*, vol. 49, no. 8, pp. 812–822, Aug. 2002.

[22] G. Tiberi, N. Ghavami, D. J. Edwards, and A. Monorchio, "Ultrawideband microwave imaging of cylindrical objects with inclusions," *IET Microw., Antennas Propag.*, vol. 5, no. 12, pp. 1440–1446, 2011.

[23] R. P. Porter and A. J. Devaney, "Holography and the inverse source problem," *J. Opt. Soc. Amer.*, vol. 72, no. 3, pp. 327–330, 1982.

[24] A. J. Devaney and R. P. Porter, "Holography and the inverse source problem. Part II: Inhomogeneous media," *J. Opt. Soc. Amer. A, Opt. Image Sci.*, vol. 2, no. 11, pp. 2006–2012, 1985.

[25] N. Ghavami, P. P. Smith, G. Tiberi, D. Edwards, and I. Craddock, "Non-iterative beamforming based on Huygens principle for multistatic ultra-wide band radar: Application to breast imaging," *IET Microw., Antennas Propag.*, vol. 9, no. 12, pp. 1233–1240, Sep. 2015.

BILAL KHALID received the bachelor's (BET) degree in electrical and telecommunications engineering from the COMSATS University of Information and Technology, Islamabad, Pakistan, and the M.Sc. degree in electrical and electronics engineering from London South Bank University, in 2019. He is currently a Ph.D. Researcher at the School of Engineering, London South Bank University. He has experience in electrical telecommunications field. He has handful experience in electromagnetics, ultra-wideband (UWB) microwave medical imaging, and skilled in MATLAB. His specialization is in healthcare technology, and designing imaging algorithms for affordable UWB microwave imaging devices for diagnostic purposes. He has experience in performing experiments and fabrication of the phantoms for MWI and part of ongoing research on lung cancer detection using UWB.

BANAFSHEH KHALESI received the Master of Science (M.Sc.) degree (Hons.) in physics (electrical and electronic engineering, biomedical engineering) from the University of Tehran, and the Ph.D. degree from London South Bank University, London, U.K. She is currently a Researcher at the School of Engineering, London South Bank University. She is a Scientific Team Member at UBT U.K. Division Company, London. She is specializing in the design and development of novel affordable medical technologies and non-invasive diagnosis imaging. Her research interests include healthcare technology, investigating new techniques for diagnostic application through ultra-wide band specifically, in the field of medical imaging. She authored some journals and conference papers on various applications of microwave imaging, including breast cancer, skin cancer, bone fracture, bone lesion detection, brain stroke, and lung imaging.

NAVID GHAVAMI received the B.Eng. degree (Hons.) in electrical and electronics engineering from King's College London, in 2009, and the Ph.D. degree from the University of Oxford, in 2013. He is currently the Co-Founder of the start-up UBT-Umbria Bioengineering Technologies founded in February 2015 in Italy and now with subsidiary in London, U.K. He has published over 40 articles on various applications of microwave imaging, including breast and skin cancer detection, brain stroke detection, and food imaging applications. He received seven university-wide prizes, including an IEEE Prize for best final-year project in the field of telecommunications during his studies at King's College London.

LORENZO SANI received the Ph.D. degree in physics from the Department of Physics and Geology (FISGEO), University of Perugia. He worked as a Research and Development Manager at MATE srl for the development of infrared spectrometers, optics. In January 2013, he joined the FISGEO through a UBT Fellowship working on the development of the first MammoWave prototype, performing several technical test on electronics and automation aspects, optimizing the algorithm with the data analysis. This work allowed UBT Team to identify the solutions for the prototype upgrades. He is currently working on the continuous development of the MammoWave, performing technical test on electronics and automation aspects, optimizing the algorithm with the data analysis.

ALESSANDRO VISPA graduated in physics from the Department of Physics and Geology (FISGEO), University of Perugia. He received the Ph.D. degree in characterization crystals and nano-crystalline materials from the Polytechnic University of Catalunya, in November 2016. After his Ph.D. degree, he joined the Scientific Team of UBT, working as a Data Analyst and a algorithm development in the context of the ongoing and future clinical trials.

MARIO BADIA received the bachelor's degree in telecommunications and electronics engineering from the Universidad de Oriente, Cuba, in 2016, with focus on software engineering, machine learning, digital signal processing and computer networks. He matured a solid experiences as a Telecommunication Engineer (ETECSA, Cuba) and as a Software Developer (Micra Software & Services Srl, Italy). In 2019, he joined UBT Srl, working in the development of radio-frequencies integrated solutions for biomedical applications, signal processing, and data analysis using machine learning algorithms.

SANDRA DUDLEY received the Ph.D. degree in physics from the University of Essex, U.K. She is currently a Professor of communication systems and the Director of Research with the School of Engineering. She investigates areas ranging from wireless sensor networks, remote sensing, non-wearable technology, and imaging. Augmenting that she also carries out research in data processing of the signals from such systems aiming towards complete platforms ready for upscaling. She manages Ph.D.'s and research associates in the above areas. She collaborates and leads on a number of U.K., EU, and IUK research grants with applications in remote user monitoring and data processing. Her research interests include low power and remote sensing schemes has led to adaptive optical-wireless systems research and the development of smart strategies for inherent physical networks, in particular a world record with BT research on lowest power broadband systems for last mile access broadband systems.

MOHAMMAD GHAVAMI (Senior Member, IEEE) is currently a Professor of telecommunications with London South Bank University, London, U.K. Prior to this appointment; he was with King's College London, London, from 2002 to 2010, and Sony Computer Science Laboratories, Tokyo, Japan, from 2000 to 2002. He has authored the books, namely, *Ultra-Wideband Signals and Systems in Communication Engineering* and *Adaptive Antenna Systems*. He has published over 170 technical articles mainly related to ultra-wideband (UWB) and its medical applications. He holds three U.S. patents and one European patent. He received the esteemed European Information Society Technologies Prize in 2005 and two invention awards from Sony. He has been a Guest Editor of the *IET Proceedings—Communications*, the Special Issue on Ultra-Wideband Systems, and an Associate Editor of the Special Issue of the *IEICE Journal on UWB Communications*.

GIANLUIGI TIBERI graduated in telecommunications engineering from the University of Pisa, Italy. He received the master's degree from King's College London, the Ph.D. degree in information engineering from the University of Pisa, and the Ph.D. degree from the University of Oxford, through a Marie Curie Intra European Fellowships for Career Development, Seventh Research Framework Program.

He is currently a Researcher at the School of Engineering, London South Bank University, London, U.K., after awarding a H2020 MSCA-IF-2017. He matured a solid experience in the applied electromagnetics and microwave imaging for medical application. He has authored more than 80 journals and conference papers. He was a Co-Lecturer of electromagnetics for medical applications at biomedical engineering with the University of Pisa. He holds two patents in medical imaging. He is the inventor of MammoWave (apparatus for testing the integrity of mammary tissues). He is the Co-Founder and the Scientific Leader of the start-up UBT—Umbria Bioengineering Technologies founded in February 2015 in Italy and now with a subsidiary in London.